Available online at www.sciencedirect.com

ScienceDirect

Journal of Magnesium and Alloys 12 (2024) 1554–1565

www.elsevier.com/locate/jma

Full Length Article

Tailoring the microstructure of Mg-Al-Sn-RE alloy via friction stir processing and the impact on its electrochemical discharge behaviour as the anode for Mg-air battery

Jingjing Liu[a], Hao Hu[b], Tianqi Wu[a], Jinpeng Chen[a], Xusheng Yang[c], Naiguang Wang[a,*], Zhicong Shi[a,*]

[a] School of Materials and Energy, Guangdong University of Technology, Guangzhou 510006, China
[b] Hunan Institute of Metrology and Test, Changsha 410014, China
[c] Department of Industrial and Systems Engineering, The Hong Kong Polytechnic University, Hung Hom, Kowloon, Hong Kong, China

Received 2 April 2022; received in revised form 17 June 2022; accepted 18 July 2022
Available online 20 September 2022

Abstract

Constructing the magnesium alloy with fine grains, low density of dislocations, and weak crystal orientation is of crucial importance to enhance its comprehensive performance as the anode for Mg-air battery. However, this unique microstructure can hardly be achieved with conventional plastic deformation such as rolling or extrusion. Herein, we tailor the microstructure of Mg-Al-Sn-RE alloy by using the friction stir processing, which obviously refines the grains without increasing dislocation density or strengthening crystal orientation. The Mg-air battery with the processed Mg-Al-Sn-RE alloy as the anode exhibits higher discharge voltages and capacities than that employing the untreated anode. Furthermore, the impact of friction stir processing on the electrochemical discharge behaviour of Mg-Al-Sn-RE anode and the corresponding mechanism are also analysed according to microstructure characterization and electrochemical response.

Keywords: Magnesium anode; Electrochemical discharge behaviour; Mg-air battery; Friction stir processing.

1. Introduction

Magnesium is suitable to serve as the anodes for seawater activated battery and Mg-air battery because of its negative standard electrode potential of −2.37 V (vs. SHE) and large Faradaic capacity of 2.2 A h g^{-1} [1,2]. As an active substance inside the cell system, magnesium anode exerts a vital role in affecting the discharge capacity and voltage [3], and it is as important as the air cathode for boosting the comprehensive battery performance, thus having received increasing attention recently [3–5]. However, the oxidation products ($Mg(OH)_2$) attached on anode surface impede the discharge process and hence positively shift the potential of magnesium [6,7], causing the voltage attenuation with prolonged discharge time. Moreover, the self-corrosion of magnesium during discharge could promote the evolution of hydrogen with the shedding of metallic particles (chunk effect), therefore decreasing the anodic efficiency and discharge capacity [4,8,9]. Both the two issues limit the wide application of aqueous power sources based on magnesium anodes.

Alloying magnesium with other elements could facilitate the spalling of oxidation products and suppress the self-corrosion [4,5]. Consequently, a lot of magnesium alloys such as Mg-Ca-In, Mg-Al-Zn-(RE) (RE = rare earths), Mg-Al-Sn-(RE), Mg-Bi-Ca, and Mg-Sn-Zn-Ag are fabricated to act as the anodes for Mg-air battery [1,6,7,10–12]. Based on the compositional optimization, several approaches including plastic deformation and heat treatment are also adopted to

* Corresponding authors.
E-mail addresses: wangnaiguang@gdut.edu.cn (N. Wang), zhicong@gdut.edu.cn (Z. Shi).

https://doi.org/10.1016/j.jma.2022.07.016

refine the grains of magnesium alloys and achieve the dispersive second phases, respectively, and these microstructure features are normally responsible for the enhanced anode performance [2,10,13]. However, because of poor plastic deformability, the conventional deformation (e.g., rolling or extrusion) of magnesium alloys is carried out at elevated temperature, which cannot significantly refine the grains. Moreover, rolling or extrusion usually creates high dislocation density and strong grain orientation. The former could accelerate the self-corrosion of magnesium alloys [4,9] whilst the latter is unfavourable for enhancing the comprehensive anode performance, as (0001) basal texture results in the weak activity during discharge while (10−10)/(11−20) oriented grains give rise to the fast corrosion at open circuit potentials (OCPs) [14,15]. Annealing at appropriate temperature after rolling usually decreases the dislocation density and maintains the refined grains [16]; however, the crystal orientation can hardly be weakened via subsequent annealing [17].

Thus, it is crucial to find relatively unconventional approaches for constructing the magnesium anode with fine grains, low dislocation density, and weak crystal orientation. Previous work showed that rapid solidification of liquid alloy with a thick-walled copper mould and spark plasma sintering of the alloy powder that had been treated via high-energy ball milling can obviously refine the grains of magnesium alloys without increasing dislocation density or strengthening crystal orientations [2,10]. However, the two approaches can only make the anode samples with small dimensions, whereas large-sized anodes are vital to the practical applications of Mg-air battery.

Friction stir processing is a solid-state grain refinement technique appropriate for the large bulk materials; it employs a rotating tool inserted into the base metal (such as aluminium or magnesium alloys) and translates this tool along the desired trajectory, hence causing severe plastic deformation together with grain refinement [18]. Patel et al. [19] modified the 6.35 mm thick AZ31B magnesium alloy by adopting friction stir processing and achieved the homogenous grain refinement throughout the thickness including top, middle, and bottom. Generally, this technique can enable the production of repeatable and homogeneous microstructures via carefully controlling the processing parameters [20,21]. Different from other plastic deformation methods, friction stir processing could be carried out at room temperature or even in cooling media such as water or liquid nitrogen, thus significantly refining the grains of magnesium alloys [19,22,23]. Moreover, based on reasonable setting of the parameters, it also weakens the crystal orientations in magnesium alloys and the dislocation density exhibits almost no increasing [22–24]. However, until recently, friction stir processing is dominantly employed in welding the metals, whereas its impact on the modification of magnesium anodes has received less attention.

In this work, we use friction stir processing to tailor the microstructure of Mg-Al-Sn-RE alloy and investigate its discharge behaviour as the anode for Mg-air battery. In this alloy, aluminium and tin can work together to enhance the anode performance [25] and activate magnesium via dissolution-redeposition mechanism [10], while cerium and yttrium strengthen the corrosion resistance at OCPs and favour the uniform dissolution of electrode during discharge [10,26]. The purpose of this work is to find a facile route to prepare the magnesium anode with refined grains, low dislocation density, and weak crystal orientation for enhancing its comprehensive discharge performance. Moreover, the electrochemical discharge mechanism of the processed Mg-Al-Sn-RE anode is also analysed based on microstructure characterization and electrochemical response.

2. Experimental procedure

2.1. Materials preparation

Mg-Al-Sn-RE alloy with a nominal composition of Mg-6 wt.% Al-1 wt.% Sn-0.2 wt.% Ce-0.2 wt.% Y was prepared via melting and casting. Specifically, the weighted magnesium ingot (99.99 wt.%) was melt in a resistance furnace at 720°C under the protection of covering agent and argon. The weighted aluminium (99.99 wt.%), tin (99.99 wt.%), Mg-20 wt.% Ce, and Mg-20 wt.% Y ingots were then added into the liquid magnesium. After 10 min, the molten alloy was stirred and poured into a steel mould to obtain the as-cast specimen (200 mm × 150 mm × 20 mm), of which the burning loss was less than 1%.

The as-cast Mg-Al-Sn-RE sample was homogenized at 400 °C for 24 h and quenched in water. The homogenized alloy (denoted as H) was cut into a size of 200 mm × 150 mm × 10 mm, and then subjected to friction stir processing with a pressure of 1.5 ton at room temperature, as schematically displayed in Fig. 1(a). The diameters of shoulder and pin were 18 mm and 6 mm, respectively, and the pin length was 7 mm. The tool moved circuitously on the surface (200 mm × 150 mm) of H for one-pass with a rotation rate of 500 rpm and a traverse speed of 100 mm min^{-1}, and the trajectory of moving tool was depicted in Fig. 2(a). The processing did not stop until the deformation area had spread all over the entire surface with a depth of about 7 mm. The Mg-Al-Sn-RE alloy after friction stir processing was named as FSP, of which the stir zone was chosen as the study subject.

2.2. Microstructure characterization

The microstructures of H and FSP were characterized systematically via various methods. An X-ray diffractometer (XRD; D/MAX-Ultima IV) with Cu Kα radiation was employed for measuring the X-ray diffraction patterns, and the 2θ was scanned from 20° to 80° at a scanning rate of 2° min^{-1}. The surfaces of these samples were mechanically ground with 400#, 1000#, 2000#, and 5000# SiC abrasive papers and polished by using SiC grinding paste; their microstructures were then observed with a scanning electron microscope (SEM; S-3400). The above surfaces were further treated via an Argon ion polisher (Leica EM RES 102) at 5, 4, and 3 keV for 1 h, respectively, and then monitored

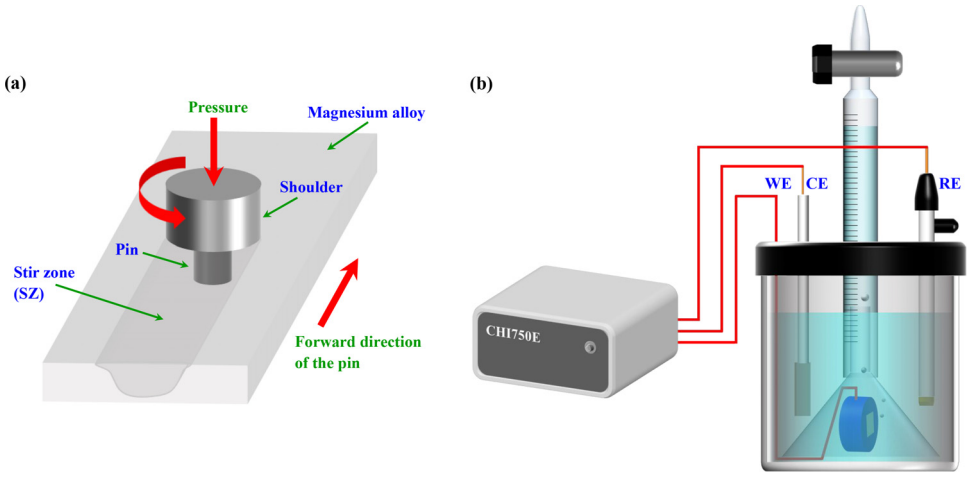

Fig. 1. Schematics of (a) friction stir processing and (b) the devices used for measuring the evolved hydrogen during discharge.

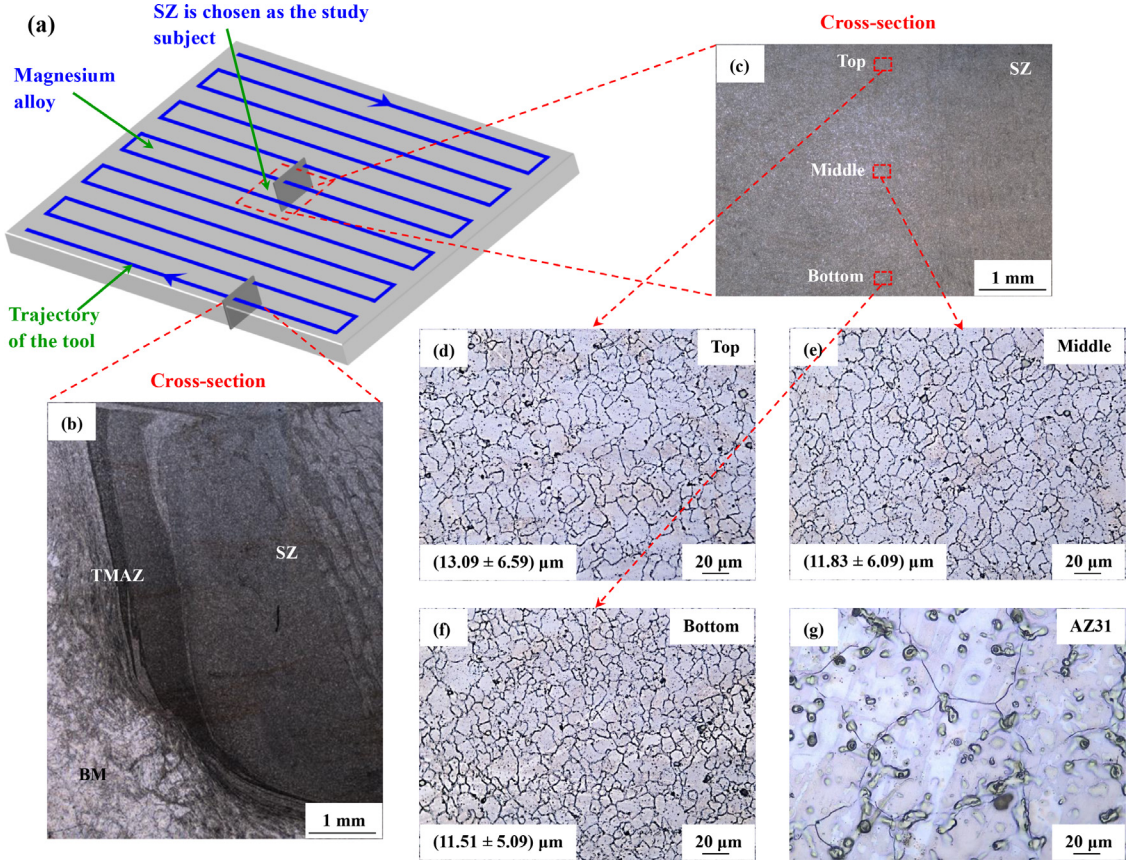

Fig. 2. (a) Trajectory of the tool during friction stir processing, cross-section macrograph in the edge (b) and centre (c) areas of processed sample, magnified images of (d) top, (e) middle, and (f) bottom regions in (c), and (g) microstructure of commercial AZ31 magnesium alloy. All these images are obtained via OM, while BM is base material, SZ is stir zone, and TMAZ is thermo-mechanically affected zone.

through a FEI Quanta 650 F SEM equipped with an electron backscatter diffraction (EBSD) probe. The scan step sizes for H and FSP were 4 and 1 μm, respectively. During the clean-up procedure of EBSD data, standard routine is employed and the points removed are fixed by filling in using copies of neighbouring points [27]. Additionally, the two specimens were also ground to a thickness of 0.08 mm and subjected to Argon ion-milling; they were characterized in detail by adopting a transmission electron microscope (TEM; FEI Talos F200X). To reveal material flow and different microstructural zones driven by friction stir processing, the ground and polished cross-section in the edge and centre areas of the sample (Fig. 2(a)) were etched with the mixed solution of 35 mL distilled water, 1 nitric acid, 1 mL acetic acid, and 1 g

oxalic acid, and then observed via an optical microscope (OM; DMI8) with different magnifications. The OM microstructure of commercial AZ31 (Mg-3 wt.% Al-1 wt.% Zn) magnesium alloy in as-cast state was included here.

2.3. Electrochemical and battery tests

The electrochemical tests of H and FSP were performed by using a CHI750E electrochemistry workstation. Moreover, AZ31 (as-cast) usually adopted as the anode for commercial Mg-air battery was also considered for comparison. Each specimen with a surface region of 10 mm × 10 mm was ground and served as the working electrode (WE). A platinum slice along with a saturated calomel electrode (SCE) acted as the counter electrode (CE) and reference electrode (RE), respectively. The electrolyte was 3.5 wt.% NaCl aqueous solution, in which these WEs had been immersed for 10 min before electrochemical measurements to obtain stable OCPs. The polarization curves were measured by scanning the potential from −1.9 V (vs. SCE) in anodic direction at 1 mV s^{-1}. The electrochemical impedance spectra (EIS) were recorded at OCPs with an amplitude of 10 mV and a frequency range of 10^5-0.05 Hz. The evolved hydrogen at OCPs and in the course of galvanostatic discharge were collected by using the devices schematically shown in Fig. 1(b). The testing period during discharge was 180 min whilst that at OCPs was 48 h since the evolution of hydrogen could enter steady state. The mass loss caused by hydrogen evolution was then calculated via the following equation [8]:

$$M_H = 0.994 \times V_H \times t \quad (1)$$

where M_H (mg cm^{-2}) was the mass loss associated with the evolved hydrogen, V_H (ml cm^{-2} h^{-1}) was the hydrogen evolution rate, and t (h) was the testing time.

H, FSP, and AZ31 were used as the anodes to assemble the Mg-air batteries based on a home-made cell. The electrolyte was 3.5 wt.% NaCl aqueous solution and a commercial air electrode with MnO_2/C catalyst was employed as the cathode. The distance between the two electrodes was 10 mm and they have the same reaction area of 10 mm × 10 mm. The performance of Mg-air batteries with different anodes was evaluated by using a LANHE-CT2001A battery testing system. Their potential-time curves were measured during galvanostatic discharge at different current densities; the anodic efficiency at each current density was calculated according to the following equation:

$$\eta = \frac{M_t}{M_a} \times 100\% \quad (2)$$

where η was anodic efficiency; M_t and M_a were theoretical and actual mass losses during discharge, respectively. M_a (mg cm^{-2}) was obtained through weighing method with chromic acid removing the oxidation products, and M_t (mg cm^{-2}) was calculated based on Faraday's law [9]:

$$M_t = 1000 \times \frac{J \times t}{F \times \sum\left(\frac{x_i \times n_i}{m_i}\right)} \quad (3)$$

where J was impressed current density (A cm^{-2}), t was discharge period (36,000 s), F was Faraday constant (96,485 C mol^{-1}), x_i, n_i, and m_i were mass fraction, ionic valence, and molar mass (g mol^{-1}) of element i. The mass loss related to chunk effect (M_c) was then estimated by

$$M_c = M_a - M_t - M_H \quad (4)$$

and M_c could reflect the detachment of metallic particles. The discharge capacity was calculated by adopting the following equation:

$$C = \frac{1000}{3600} \times F \times \sum\left(\frac{x_i \times n_i}{m_i}\right) \times \eta \quad (5)$$

where C was discharge capacity (mA h g^{-1}). The discharged anode surfaces before and after cleaning the oxidation products by chromic acid were observed via an S-3400 SEM.

At least three parallel tests were performed for each specimen to ensure the reproducibility of data.

3. Results and discussion

3.1. Microstructures

Fig. 2(b) presents the cross-section macrograph of the edge area in FSP. Since the processed region spreads all over the entire specimen, base material (BM) can only be clearly distinguished at the edge area, where thermo-mechanically affected zone (TMAZ) along with stir zone (SZ) are also identified. Material flow driven by rotating tool occurs in the SZ, of which the heat dissipation and the material flow can influence the adjacent TMAZ [18]. In contrast, the BM is less affected and the defects are not obvious in the processed sample.

The cross-section macrograph displayed in Fig. 2(c) manifests that the SZ occupies the whole central area. The top, middle, and bottom regions in Fig. 2(c) consist of equiaxed grains, as given in Fig. 2(d), (e), and (f), respectively, thus demonstrating dynamic recrystallization during friction stir processing. The grain sizes in the three regions are measured by using linear intercept method [28]. At least 200 grains in each region are selected, and the results indicate that the average grain sizes in top, middle, and bottom of SZ are 13.09 ± 6.59, 11.83 ± 6.09, and 11.51 ± 5.09 μm, respectively. Accordingly, grain size deviation is not obvious and temperature gradient across the thickness of SZ is small, contributing to the relatively uniform and fine grains in Mg-Al-Sn-RE alloy [29–31]. Fig. 2(g) presents the OM microstructure of AZ31, which are composed of α-Mg matrix and β-$Mg_{17}Al_{12}$ phase along the grain boundaries/within the grains.

The XRD patterns shown in Fig. 3(a) manifest that both H and FSP only exhibit the diffraction peaks of magnesium, ascribed to the low contents of other elements together with their solid solution in magnesium matrix. Each peak is associated with a crystal plane of magnesium, and the difference among the peak intensities is not obvious for the two specimens. Hence, the crystal orientations are relatively weak for

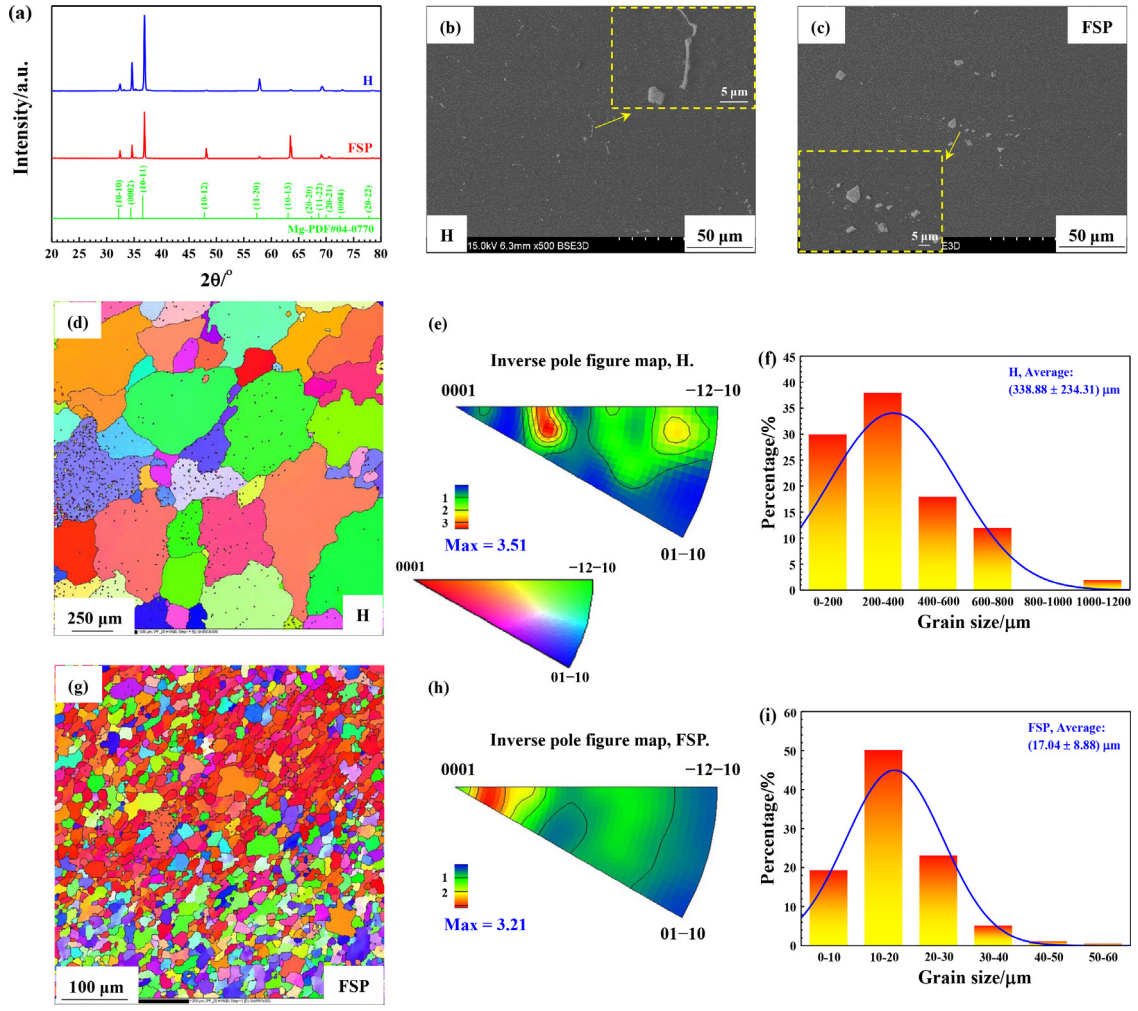

Fig. 3. (a) XRD patterns, SEM images of (b) H and (c) FSP, crystal orientation maps of (d) H and (g) FSP, inverse pole figures (IPFs) of (e) H and (h) FSP, and grain size distributions of (f) H and (i) FSP.

both H and FSP. Moreover, the (10−12) and (10−13) peaks less visible in H have obviously higher intensity in FSP, of which the (11−20) intensity is weakened in contrast with that of H. According to Xu et al. [32] and Bian et al. [33], (10−12) and (10−13) planes are the tensile and compression twins induced by friction stir processing, respectively. Because <11−20> is easy slip direction [32], the severe plastic deformation during friction stir can reduce the intensity of (11−20) plane. The SEM images presented in Fig. 3(b) and (c) reveal the dispersive second phases in the two specimens. They are mainly identified as rare earth γ phase (Al_2Ce/Al_2Y) and long period stacking order (LPSO) phase by using TEM, and the corresponding details will be given later.

The crystal orientation maps obtained via EBSD techniques are presented in Fig. 3(d) and (g), which can reveal the grain sizes and orientations of the two specimens. The grains in EBSD data are defined as the areas surrounded by high angle grain boundaries (≥15°) [34], and their sizes are also analysed with linear intercept method. The reason is that although the EBSD method is automated, great care must be taken in data analysis to identify and handle consistently small size values [35]. It can be observed that H has larger grains with random orientations (Fig. 3(d)), whereas the grains of FSP are greatly refined and its local areas exhibit strong crystal orientations (Fig. 3(g)). However, the inverse pole figure maps based on EBSD techniques manifest weak orientation intensities in the whole maps of the two specimens, as displayed in Fig. 3(e) and (h). The orientation intensity of FSP is only 3.21, which is obviously smaller than those of other magnesium alloys treated through rolling [36], extrusion [9], and the friction stir processing with different parameters or tool dimensions [37,38]. Moreover, Fig. 3(f) and (i) also unravel the uniform grain sizes in H and FSP, respectively, and the grains refined with friction stir processing are more uniform than those modified by employing extrusion [9], ball milling and spark plasm sintering [2].

Thereby, reasonably controlling the tool dimensions, trajectory, and corresponding parameters enables friction stir processing to generate the uniformly refined grains of magnesium alloy without strengthening its crystal orientations. It is also known from Fig. 3(i) that the average grain size of FSP is 17.04 ± 8.88 μm, which is slightly larger than that

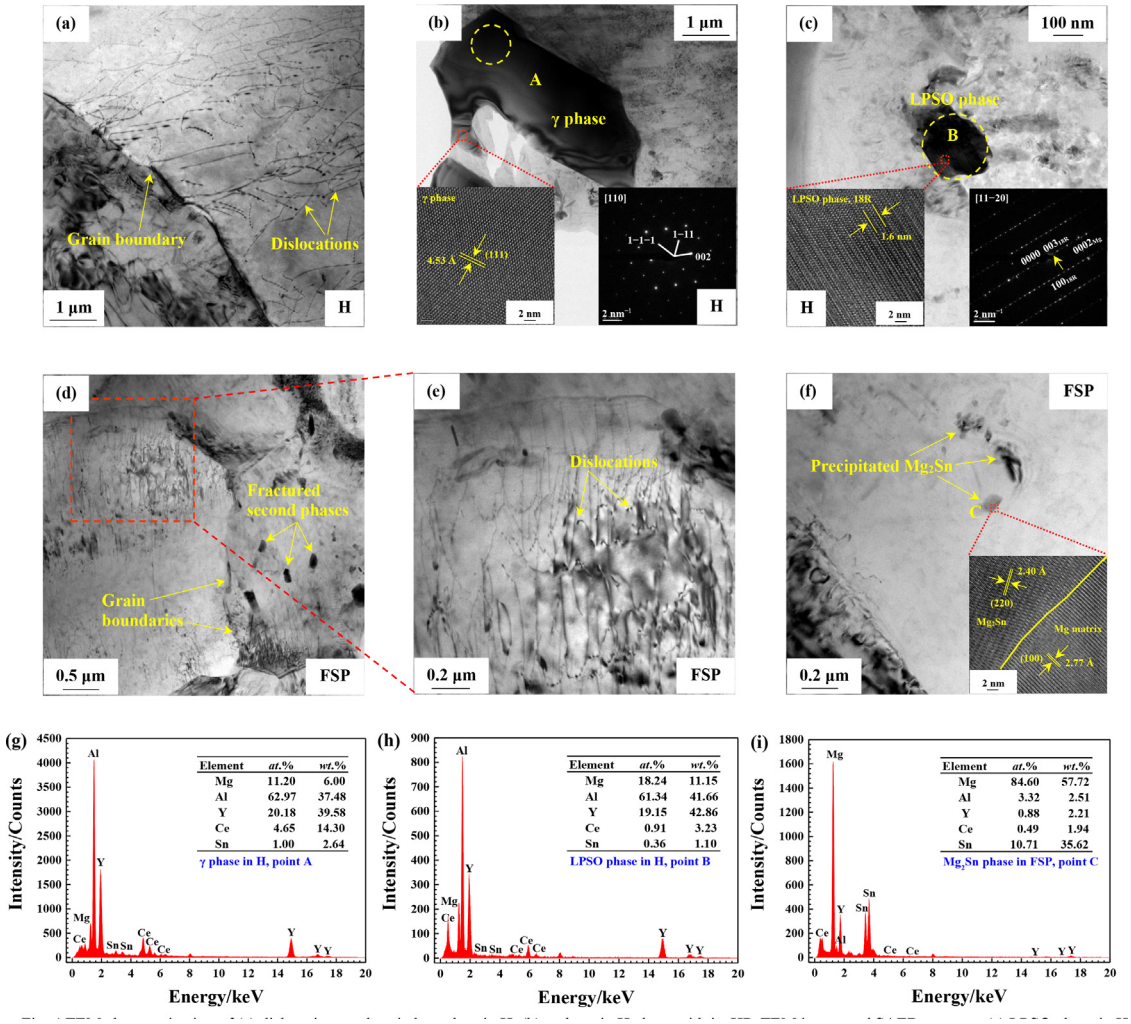

Fig. 4. TEM characterization of (a) dislocations and grain boundary in H, (b) γ phase in H along with its HR-TEM image and SAED patterns, (c) LPSO phase in H along with its HR-TEM image and SAED patterns, (d) grain boundaries and fractured second phases in FSP, (e) dislocations in FSP, (f) Mg_2Sn phase in FSP along with its HR-TEM images and SAED patterns, (g) EDX result of γ phase in H (point A), (h) EDX result of LPSO phase in H (point B), and (i) EDX result of Mg_2Sn phase in FSP (point C).

based on OM image (Fig. 2(d)). This result is mainly ascribed to the different locations that are sampled. Taking the error bars into consideration, the disparity of grain sizes is not obvious.

The microstructure details of H and FSP are studied with TEM analysis. H exhibits low density of dislocations (Fig. 4(a)); the γ and LPSO phases are also seen in its matrix, as presented in Fig. 4 (b) and (c), respectively. The high-resolution (HR) TEM images along with the selected area electron diffraction (SAED) patterns inserted in Fig. 4(b) and (c) could offer the structure information of the two phases, and their compositions obtained via energy-dispersive X-ray spectroscopic (EDX) analysis are given in Fig. 4(g) and (h). According to Kishida et al. [39], the formation of LPSO is caused by the interaction of cerium/yttrium and aluminium during solidification process, and the EDX result (Fig. 4(h)) unravels the high contents of aluminium and rare earths in LPSO phase.

FSP still presents low dislocation density and its second phases (e.g., γ and LPSO) are fractured during the friction stir processing, as observed in Fig. 4(d) and (e). In contrast with H, more grain boundaries are created in FSP (Fig. 4(d)) and a new phase of Mg_2Sn are also precipitated, as shown in Fig. 4(f). The inserted HR-TEM image clearly unveils the microstructure details of Mg_2Sn phase, and its compositional information obtained via EDX analysis are given in Fig. 4(i). Because of the low content of tin in Mg-Al-Sn-RE alloy, the homogenization at 400 °C for 24 h gives rise to its solid solution in magnesium matrix [40,41]. The precipitation of Mg_2Sn in FSP is attributed to the heat release during friction stir processing, which also promotes the dynamic recrystallization and hence reduces the density of dislocations. This means that friction stir processing in air condition at room temperature could sustain the relatively low dislocation density in magnesium alloys, as consistent with several literature studies [23,38,42].

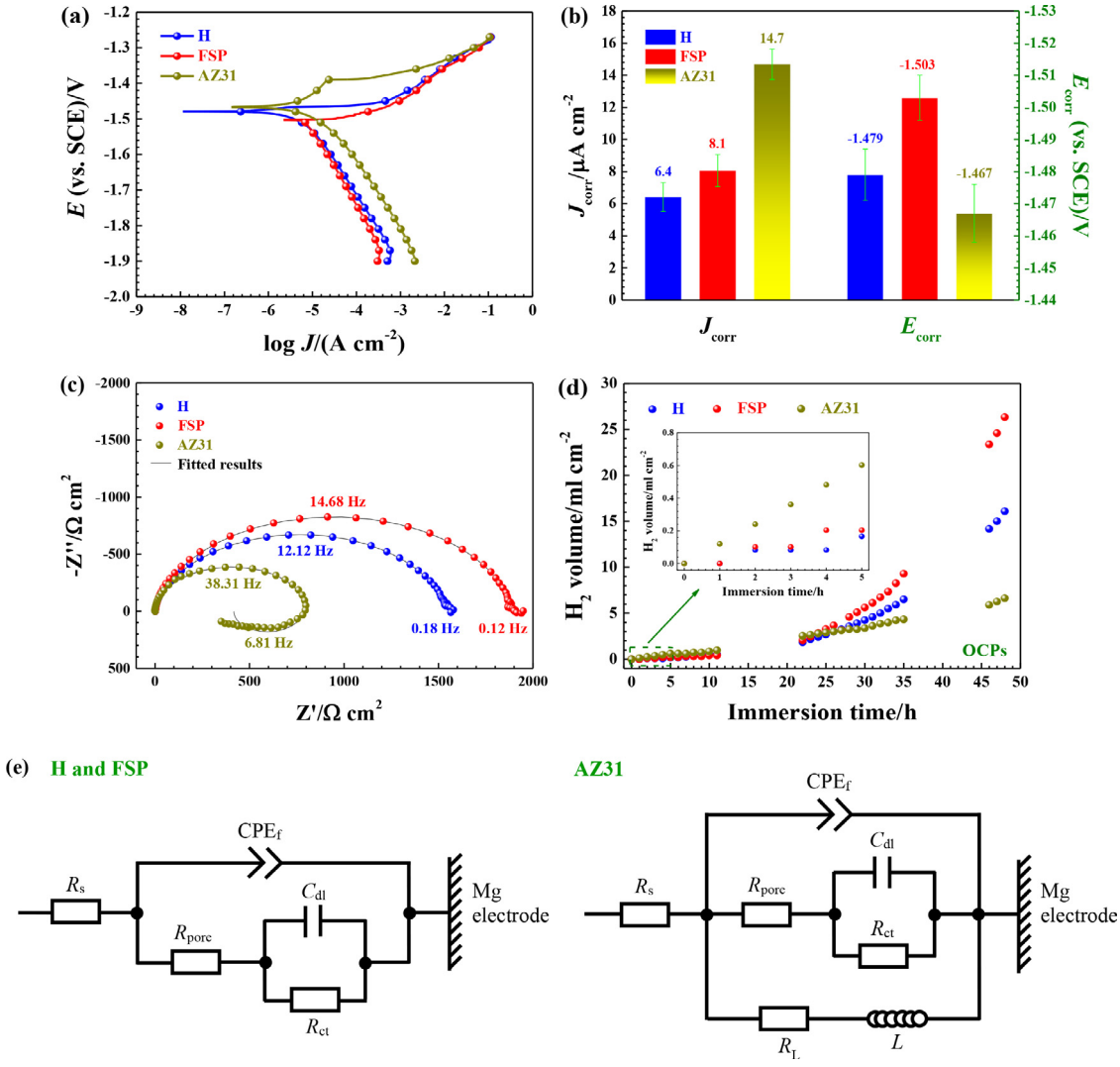

Fig. 5. (a) Polarization curves, (b) corrosion current densities (J_{corr}) and corrosion potentials (E_{corr}), (c) EIS at OCPs, (d) hydrogen evolution behaviour at OCPs, and (e) equivalent circuits for fitting the EIS.

3.2. Electrochemical discharge behavior

The polarization curves shown in Fig. 5(a) indicate the more negative corrosion potential (E_{corr}) of FSP compared with those of H and AZ31. In addition, FSP also gives relatively smaller cathodic current density and larger anodic current density than other samples, suggesting that the magnesium anode with fine grains, low dislocation density, and weak crystal orientation can inhibit the evolution of hydrogen during cathodic polarization and boost the dissolution when applied anodic polarization. The corrosion current density (J_{corr}) of each specimen is obtained via extrapolating the linear part of cathodic branch back to its E_{corr}, and the result is shown in Fig. 5(b). AZ31 displays the largest J_{corr} among the three specimens, whereas the values of J_{corr} exhibit no obvious difference between H and FSP within the error ranges. Hence, at the initial stage in 3.5 wt.% NaCl, H and FSP possess strong corrosion resistance than AZ31.

The EIS shown in Fig. 5(c) are also consistent with the results of J_{corr}. H and FSP display larger diameters in EIS, whereas the curve of AZ31 obviously shrinks. The equivalent circuits depicted in Fig. 5(e) are employed to fit the EIS with the corresponding data summarized in Table 1. AZ31 has different circuit among the three samples, owing to the compositional difference that influences the electrochemical corrosion behaviour at OCPs. R_{pore} equals to the diameter of first semicircle, which is related to the electrolyte penetrating through the pores in $Mg(OH)_2$ film [2]. The larger R_{pore} values of H and FSP signify their stronger corrosion resistances induced by surface films, as compared with AZ31 during the initial immersion at OCPs. Moreover, the charge transfer resistance (R_{ct}) equivalent to the second semicircle diameter is obviously smaller than the R_{pore} for each sample, indicating that the $Mg(OH)_2$ film might be more important for enhancing its corrosion resistance.

Fig. 5(d) gives the hydrogen evolution behaviour at OCPs, which indicates that AZ31 suffers more severe corrosion at

Table 1
Electrochemical parameters obtained through the fitting of EIS at OCPs.

Mg electrode	R_s/(Ω cm^2)	R_{pore}/(Ω cm^2)	Y_f/(Ω^{-1} cm^{-2} s^n)	n_f	R_{ct}/(Ω cm^2)	Y_{dl}/(Ω^{-1} cm^{-2} s)
H	2	1535	1.1×10^{-5}	0.915	42	6.0×10^{-2}
FSP	2	1888	8.5×10^{-6}	0.915	20	9.0×10^{-2}
AZ31	1	815	6.2×10^{-6}	0.97	90	2.4
Mg electrode	n_{dl}	R_L/(Ω cm^2)	L/(H cm^2)	χ^2		
H	1	–	–	5.1×10^{-4}		
FSP	0.7	–	–	4.6×10^{-4}		
AZ31	1	770	110	6.9×10^{-4}		

Y_f is the parameter similar to the capacitance and n_f is an index without dimension.

the initial stage (inserted figure), as in accordance with the J_{corr} and EIS. However, long period tests unravel the obviously faster corrosion of Mg-Al-Sn-RE (especially FSP) than AZ31, possibly ascribed to the rupture of $Mg(OH)_2$ film after long time corrosion and therefore the protection effect disappears. Similar phenomenon was also discovered in the T4 treated AZ91D magnesium alloy, of which the protective film was broken down with prolonging immersion period in simulated body fluid and the corrosion rate increased rapidly [43]. As the second phases in H and FSP are dispersed well in the matrices with low dislocation densities, the more active behaviour of FSP is explained by its larger number of grain boundaries that disrupt the surface film and accelerate the dissolution at OCPs [2]. Several literature studies reported that the magnesium alloys treated by friction stir processing possess strong corrosion resistances at OCPs [44,45], and this inconformity might be caused by the difference in compositions, which give rise to the various morphologies of second phases and thus affects the corrosion behaviour.

The electrochemical discharge behaviour of H, FSP, and AZ31 as the anodes for Mg-air battery is shown in Fig. 6. The discharge plateaus follow the sequence of FSP>H>AZ31 at 1, 5, and 10 mA cm^{-2}, as confirmed by Fig. 6(a), (b), and (c), respectively. Thus, FSP exhibits stronger discharge activity than other specimens, and this result can also be predicted via the morphologies of oxidation products after the battery discharge. According to Fig. 7(a), H displays several pores on the oxidation products when discharged at 10 mA cm^{-2} for 1 h, and the magnified image unravels their irregular shapes (Fig. 7(b)). In contrast, more circular pores surrounded by the oxidation products are visible on the discharged surface of FSP (Fig. 7(c) and (d)). As a consequence, the electrolyte can fully contact with the surface and FSP retains relatively larger active electrode area. The average voltage provided by FSP at 10 mA cm^{-2} can reach 1.284 V, higher than that of the state-of-the-art Mg-Ca-In anode without the consideration of battery structures [1]. In contrast, the weaker discharge activity of AZ31 is caused by the absence of activated elements such as tin, which can strengthen the activity of magnesium through dissolution-redeposition mechanism [10]. However, AZ31 sustains a stable discharge plateau at each current density, while the voltages of H and FSP (especially H) gradually decrease with elapsed time at 5 and 10 mA cm^{-2}. This result is owing to the fact that more oxidation products are formed on the surfaces of Mg-Al-Sn-RE alloys; these products will be detached due to gravity as the discharge period is prolonged further, thus leading to the recovery of voltage plateaus. Nevertheless, further modification of the Mg-Al-Sn-RE alloys is still required for quick spalling of the oxidation products.

Since H and FSP with the same chemical compositions show low dislocation density and weak crystal orientations, their discharge activity is predominantly influenced by grain sizes. Friction stir processing significantly refines the grains of Mg-Al-Sn-RE alloy and creates a large number of grain boundaries, which can act as the channels for anodic dissolution reaction [2,46] and thus favour the formation of more pores on the oxidation products of FSP. Additionally, its fractured γ and LPSO phases together with the precipitated Mg_2Sn with small sizes also promote the spalling of oxidation products [47]. Hence, compared with H that possesses larger grains and second phases, FSP exhibits stronger discharge activity and higher voltage plateaus.

The behaviour of hydrogen evolution during the discharge process at 1, 5, and 10 mA cm^{-2} is presented in Fig. 6(d), (e), and (f), respectively. AZ31 releases less hydrogen than H and FSP at each current density, whilst the self-corrosion on FSP is suppressed compared with that on H. The lower rate of hydrogen evolution for AZ31 is attributed to the addition of zinc, which has a small exchange current density for the evolution of hydrogen and thus mitigates the self-corrosion. Since H and FSP exhibit low dislocation density and weak crystal orientation, their difference in hydrogen evolution behaviour is mainly derived from the grain sizes. In contrast with H, FSP possessing obviously finer grains displays more grain boundaries, which could serve as the barriers for restraining the evolution of hydrogen during discharge [2,46]. This phenomenon is different from the corrosion behaviour at OCPs since the impressed current during discharge leads to anodic polarization and hence obviously alters the surface conditions, giving rise to the breakdown of surface film. Under this condition, the grain boundaries with strong activity serve as the local anodic areas, whilst the intragranular regions with lower energy act as the local cathodes [2]. The large number of grain boundaries in FSP enable the formation of small cathodes/anodes ratio and hence mitigate the evolved hydrogen [2]. Moreover, the sorts and morphologies of second phases are also important to the self-corrosion of magnesium anodes during discharge. The precipitated Mg_2Sn, the fractured γ and

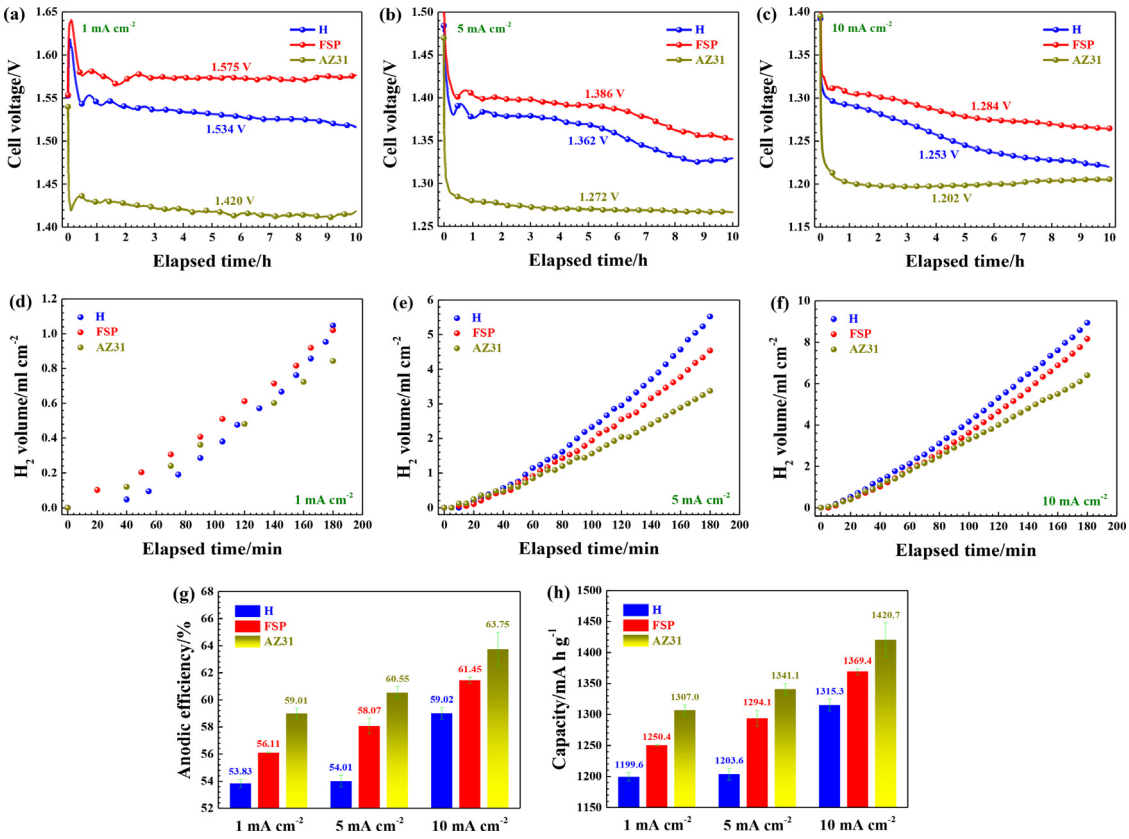

Fig. 6. Voltage-time curves of Mg-air batteries at (a) 1 mA cm^{-2}, (b) 5 mA cm^{-2}, and (c) 10 mA cm^{-2}; hydrogen evolution behaviour at (d) 1 mA cm^{-2}, (e) 5 mA cm^{-2}, and (f) 10 mA cm^{-2}; (g) anodic efficiencies and (h) capacities at different current densities.

LPSO phases possessing small sizes in FSP can effectively inhibit the micro-galvanic effect [10]. Therefore, compared with H that has larger grains and second phases, FSP shows a lower rate of hydrogen evolution when discharged at the same current density.

The anodic efficiencies and discharge capacities of H, FSP, and AZ31 are shown in Fig. 6(g) and (h), respectively. The two parameters follow the reverse sequences as that of hydrogen evolution during discharge, i.e., AZ31 with the lowest rate of hydrogen evolution gives the highest efficiency and capacity at each current density, whilst the anodic efficiency and discharge capacity of FSP are higher than those of H at the same current density, respectively. In addition to evolved gas, the self-corrosion that adversely affects the efficiency and capacity also includes the chunk effect, which is normally reflected through observing the discharged anode surface after clearing away the oxidation products. According to Fig. 7(e), H dissolves ununiformly and several local pores with large depth can be seen after 10 h discharge at 10 mA cm^{-2}. In contrast, the dissolution of FSP is relatively more uniform due to the refined grains (Fig. 7(g)). The magnified images given in Fig. 7(f) and (h) unveil many grooves on the two specimens, whereas the angular pits correlated with chunk effect [7,9,10] is less obvious. Consequently, both H and FSP only suffer the slight detachment of metallic particles during discharge. Moreover, Fig. 7(h) also reveals many grain boundaries on the discharged surface of FSP, manifesting that the grain boundaries with high energy dissolve preferentially and the large number of grain boundaries in FSP is favourable for its uniform dissolution.

The anodic efficiency of FSP at 10 mA cm^{-2} reaches (61.45 ± 0.23)%, slightly lower than that of AZ31 but still higher than those of many commercial magnesium alloys, e.g., WE43, E21, AM50, and ZE41 [8]. Since AZ31 has obviously weaker discharge activity (Fig. 6(a)–(c)) and suffers severe corrosion during the initial immersion at OCPs (Fig. 5(a)–(d)), friction stir processing is adopted to tailor the microstructure of Mg-Al-Sn-RE alloy possessing stronger discharge activity for enhancing its comprehensive anode performance.

The percentages of mass losses corresponding to the electric current (theoretical mass loss, M_t), hydrogen evolution (M_H), and chunk effect (M_c) are shown in Fig. 8. For each sample, the percentage of M_t equals to the anodic efficiency at a certain current density, whilst those of M_H and M_c are the parts of wasted magnesium anode caused by the self-corrosion during discharge. Moreover, the ratio of M_H is obviously higher than that of M_c at each current density. Thus, compared with chunk effect, hydrogen evolution is more deleterious to the anodic efficiencies and capacities of tested specimens. This phenomenon is different from what Deng et al. [8] reported that chunk effect could cause large efficiency losses up to 50% for some magnesium alloys, attributed to the differences in compositions and second phase

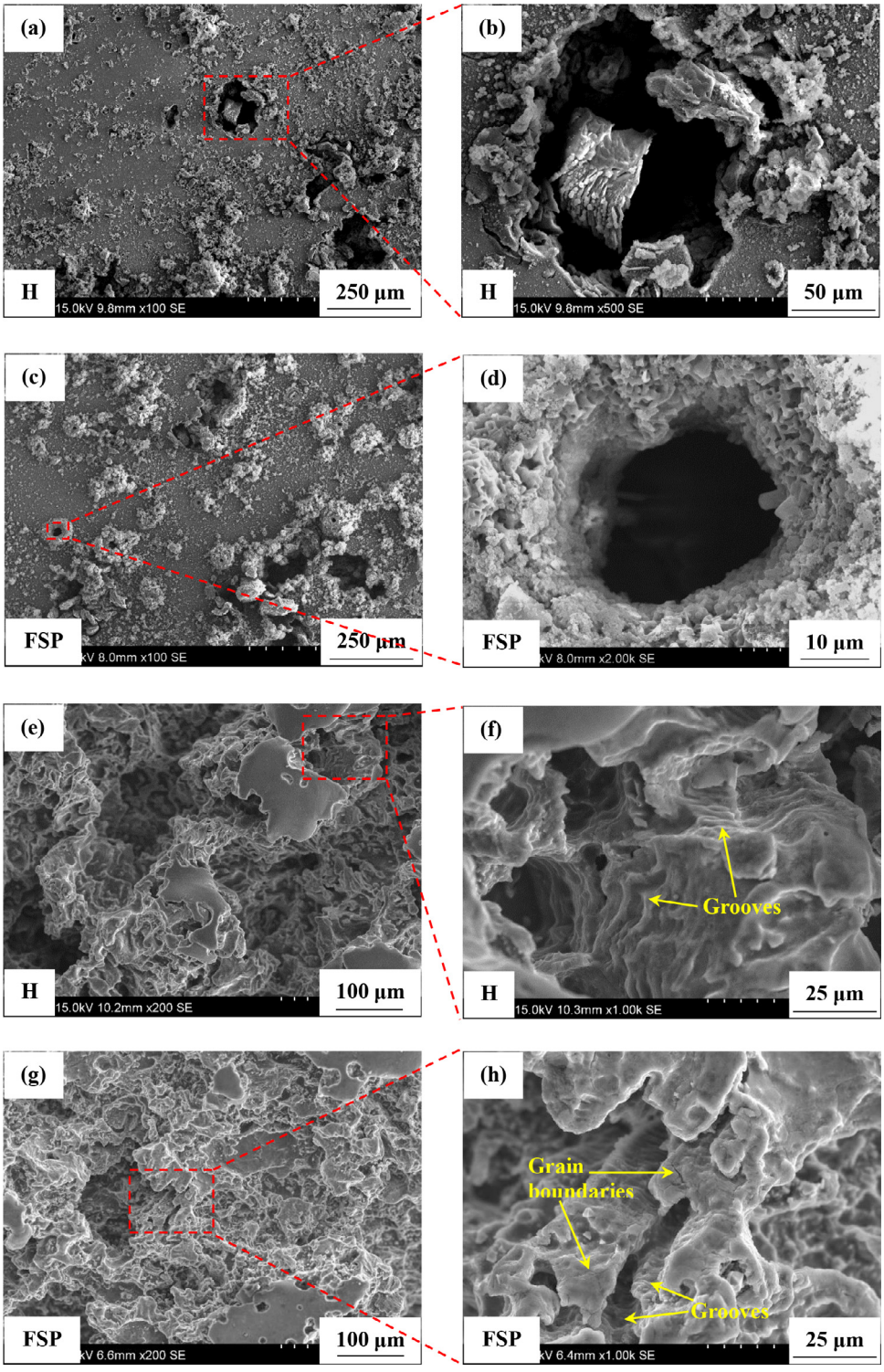

Fig. 7. Surface morphologies discharged at 10 mA cm^{-2} of (a) 1 h discharge with oxidation products for H, (b) magnified region in (a), (c) 1 h discharge with oxidation products for FSP, (d) magnified region in (c), (e) 10 h discharge cleaning oxidation products for H, (f) magnified region in (e), (g) 10 h discharge cleaning oxidation products for FSP, and (h) magnified region in (g).

fractions. The lower fractions of second phases in H and FSP suppress the metallic particles shed from the anode surface, thus mitigating the chunk effect during discharge. Despite the higher percentages of M_H, H and FSP possess lower ratios of M_c than AZ31 at each current density, manifesting that the chunk effect in H and FSP is suppressed, as in accordance with the discharged surfaces presented in Fig. 7(e)–(h). However, further work is still needed to inhibit the self-corrosion for enhancing the anodic efficiency of Mg-Al-Sn-RE alloy.

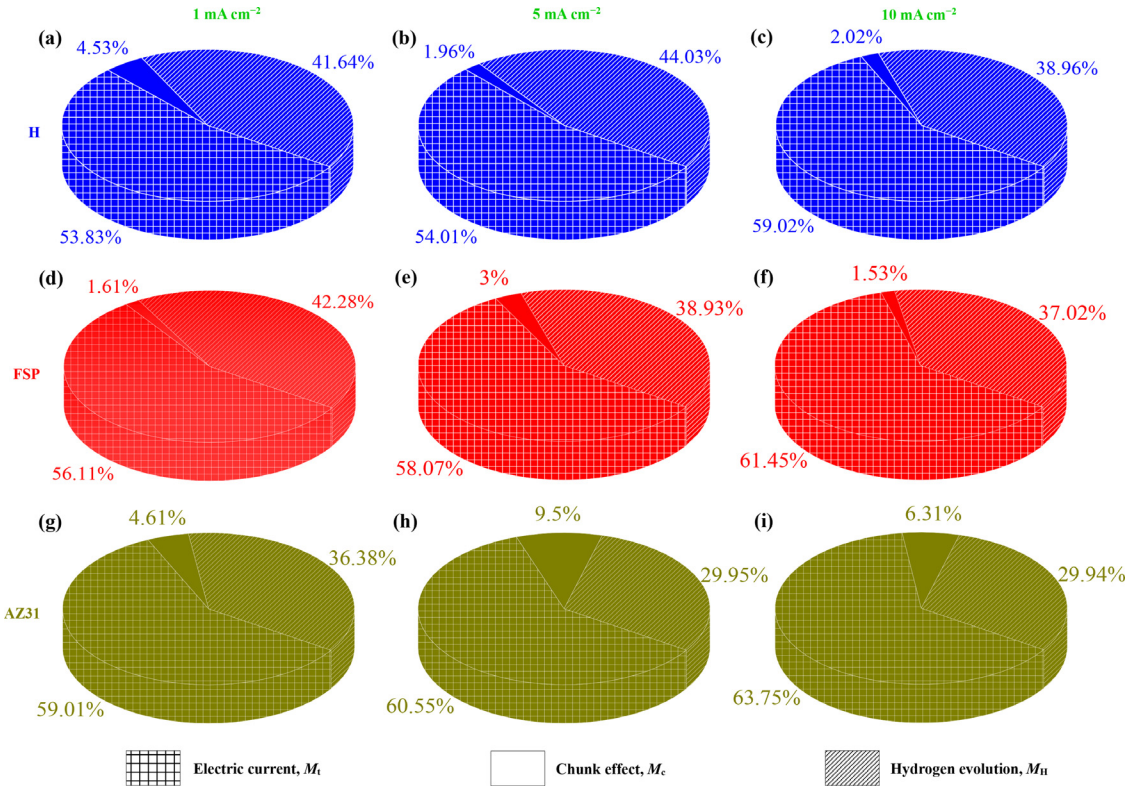

Fig. 8. Percentages of mass loss at different current densities corresponding to electric current, chunk effect (detachment of metallic particles), and hydrogen evolution (a)-(c) H, (d)-(f) FSP, and (g)-(i) commercial AZ31 magnesium alloy.

4. Conclusions

The microstructure of Mg-Al-Sn-RE alloy is tailored by using friction stir processing, and its impact on the electrochemical discharge behaviour as the anode for Mg-air battery is systematically investigated. The main conclusions can be drawn as follows:

(i) Friction stir processing greatly refines the grains of Mg-Al-Sn-RE alloy without increasing its dislocation density. Based on reasonably controlling the processing parameters, the grains of Mg-Al-Sn-RE alloy exhibit weak preferred orientation over a broad size range. However, the parameters still need to be further optimized for reducing the local intensity of crystal orientation.

(ii) The processed Mg-Al-Sn-RE alloy shows enhanced anode performance compared with the untreated alloy. The refined grains along with the fractured and precipitated second phases produced via friction stir processing not only promote the spalling of oxidation products but also suppress the evolution of hydrogen. All these aspects are responsible for the high voltage plateaus and discharge capacities of Mg-air battery that uses the processed Mg-Al-Sn-RE alloy as the anode.

(iii) The Mg-air battery with the processed Mg-Al-Sn-RE anode can provide an average voltage of 1.284 V at 10 mA cm^{-2}, which is higher than those delivered by the commercial AZ31 magnesium anode and the state-of-the-art Mg-Ca-In anode. Additionally, in contrast with AZ31, the chunk effect for Mg-Al-Sn-RE is effectively suppressed. However, further modification (such as alloying) is still warranted for the processed Mg-Al-Sn-RE anode to inhibit its evolution of hydrogen during battery discharge.

Acknowledgments

The Authors acknowledge the financial support of the National Nature Science Foundation of China (No. 52171067) and the Natural Science Foundation of Guangdong Province of China (No. 2022A1515012366).

References

[1] M. Deng, L. Wang, D. Höche, S.V. Lamaka, P. Jiang, D. Snihirova, N. Scharnagl, M.L. Zheludkevich, J. Power Sources 472 (2020) 228528.
[2] N. Wang, Y. Huang, J. Liu, X. Yang, W. Xie, Q. Cai, S. Zheng, Z. Shi, Electrochim. Acta 378 (2021) 138135.
[3] X. Liu, S. Liu, J. Xue, J. Power Sources 396 (2018) 667–674.
[4] X. Chen, X. Liu, Q. Le, M. Zhang, M. Liu, A. Atrens, J. Mater. Chem. A 9 (2021) 12367–12399.
[5] N. Wang, J. Liang, J. Liu, Q. Cai, J. Li, J. Chen, T. Huang, Z. Shi, J. Power Sources 517 (2022) 230707.
[6] X. Chen, S. Ning, Q. Le, H. Wang, Q. Zou, R. Guo, J. Hou, Y. Jia, A. Atrens, F. Yu, J. Mater. Sci. Technol. 38 (2020) 47–55.
[7] X. Liu, J. Xue, P. Zhang, Z. Wang, J. Power Sources 414 (2019) 174–182.
[8] M. Deng, L. Wang, D. Höche, S.V. Lamaka, D. Snihirova, B. Vaghefinazari, M.L. Zheludkevich, J. Power Sources 441 (2019) 227201.

[9] N. Wang, W. Li, Y. Huang, G. Wu, M. Hu, G. Li, Z. Shi, J. Power Sources 436 (2019) 226855.
[10] N. Wang, J. Liang, J. Liu, Y. Huang, H. Shao, Q. Cai, M. Hu, Z. Shi, J. Electrochem. Soc. 168 (2021) 100537.
[11] S. Cheng, W. Cheng, X. Gu, H. Yu, Z. Wang, H. Wang, L. Wang, J. Alloy. Compd. 823 (2020) 153779.
[12] X. Gu, W. Cheng, S. Cheng, H. Yu, Z. Wang, H. Wang, L. Wang, J. Electrochem. Soc. 167 (2020) 020501.
[13] H. Yang, L. Wu, B. Jiang, W. Liu, J. Song, G. Huang, D. Zhang, F. Pan, J. Mater. Sci. Technol. 62 (2021) 128–138.
[14] W. Cheng, Y. Chen, X. Gu, J. Feng, H. Yu, H. Wang, X. Niu, L. Wang, H. Li, J. Power Sources 520 (2022) 230802.
[15] N. Wang, Y. Mu, W. Xiong, J. Zhang, Q. Li, Z. Shi, Corros. Sci. 144 (2018) 107–126.
[16] N. Wang, R. Wang, C. Peng, Y. Feng, B. Chen, Corros. Sci. 64 (2012) 17–27.
[17] G.L. Song, Z. Xu, Corros. Sci. 54 (2012) 97–105.
[18] D. Sejani, W. Li, V. Patel, Crit. Rev. Solid State Mater. Sci. (2021) 1–50.
[19] V. Patel, W. Li, Y. Xu, Mater. Manuf. Process. 34 (2018) 177–182.
[20] A.N. Albakri, B. Mansoor, H. Nassar, M.K. Khraisheh, J. Mater. Process. Technol. 213 (2013) 279–290.
[21] Z.Y. Ma, Metall. Mater. Trans. A 39 (2008) 642–658.
[22] A. Shahnam, F. Karimzadeh, M.A. Golozar, S.N. Hosseini, J. Mater. Eng. Perform. 28 (2019) 4593–4601.
[23] N. Kumar, D. Choudhuri, R. Banerjee, R.S. Mishra, Int. J. Plast. 68 (2015) 77–97.
[24] Q. Yang, B.L. Xiao, D. Wang, M.Y. Zheng, K. Wu, Z.Y. Ma, J. Alloy. Compd. 581 (2013) 585–589.
[25] T. Zheng, Y. Hu, Y. Zhang, S. Yang, F. Pan, Mater. Des. 137 (2018) 245–255.
[26] Y. Feng, W. Xiong, J. Zhang, R. Wang, N. Wang, J. Mater. Chem. A 4 (2016) 8658–8668.
[27] V. Randle, Mater. Charact. 60 (2009) 913–922.
[28] A. Thorvaldsen, Acta Mater. 45 (1997) 595–600.
[29] V. Patel, W. Li, J. Andersson, N. Li, J. Mater. Res. Technol. 17 (2022) 3150–3156.
[30] V. Patel, W. Li, A. Vairis, V. Badheka, Crit. Rev. Solid State Mater. Sci. 44 (2019) 378–426.
[31] V. Patel, W. Li, X. Liu, Q. Wen, Y. Su, J. Shen, B. Fu, Mater. Sci. Eng. A 784 (2020) 139322.
[32] N. Xu, S. Cai, Q. Song, Y. Bao, J. Mater. Sci. Technol. 35 (2019) 993–997.
[33] N. Bian, F. Li, Y. Wang, C. Li, J. Mater. Eng. Perform. 30 (2021) 9215–9226.
[34] F.J. Humphreys, J. Microsc. 213 (2004) 247–256.
[35] K.P. Mingard, B. Roebuck, E.G. Bennett, M.G. Gee, H. Nordenstrom, G. Sweetman, P. Chan, Int. J. Refract. Met. Hard Mater. 27 (2009) 213–223.
[36] U.M. Chaudry, T.H. Kim, Y.S. Kim, K. Hamad, Y.G. Ko, J.G. Kim, Mater. Sci. Eng. A 762 (2019) 138085.
[37] W. Yuan, R.S. Mishra, Mater. Sci. Eng. A 558 (2012) 716–724.
[38] N. Kumar, N. Dendge, R. Banerjee, R.S. Mishra, Mater. Sci. Eng. A 590 (2014) 116–131.
[39] K. Kishida, H. Yokobayashi, H. Inui, Sci. Rep. 7 (2017) 12294.
[40] X. Huang, W. Huang, Mater. Charact. 151 (2019) 260–266.
[41] W. Cheng, Y. Bai, L. Wang, H. Wang, L. Bian, H. Yu, Materials 10 (2017) 822.
[42] W. Yuan, S.K. Panigrahi, R.S. Mishra, Metall. Mater. Trans. A 44 (2013) 3675–3684.
[43] W. Zhou, T. Shen, N.N. Aung, Corros. Sci. 52 (2010) 1035–1041.
[44] H. Seifiyan, M. Heydarzadeh Sohi, M. Ansari, D. Ahmadkhaniha, M. Saremi, J. Magnes. Alloy. 7 (2019) 605–616.
[45] Q. Liu, G.Q. Chen, S.B. Zeng, S. Zhang, F. Long, Q.Y. Shi, J. Alloy. Compd. 851 (2021) 156835.
[46] L. Fan, H. Lu, J. Power Sources 284 (2015) 409–415.
[47] Y. Song, J. Ma, Y. Li, G. Wang, C. Qin, H.R. Stock, Ionics 25 (2019) 5899–5906.